Inorganic Chemistry

Article

pubs.acs.org/IC

Topotactic Solid-State Metal Hydride Reductions of Sr_2MnO_4

Bradley C. Hernden,[†,‡] Joey A. Lussier,[†,‡] and Mario Bieringer*[,†]

[†]Department of Chemistry, University of Manitoba, Winnipeg, Manitoba R3T 2N2, Canada

Supporting Information

ABSTRACT: We report novel details regarding the reactivity and mechanism of the solid-state topotactic reduction of Sr_2MnO_4 using a series of solid-state metal hydrides. Comprehensive details describing the active reducing species are reported and comments on the reductive mechanism are provided, where it is shown that more than one electron is being donated by H^-. Commonly used solid-state hydrides LiH, NaH, and CaH_2, were characterized in terms of reducing power. In addition the unexplored solid-state hydrides MgH_2, SrH_2, and BaH_2 are evaluated as potential solid-state reductants and characterized in terms of their reductive reactivities. These 6 group I and II metal hydrides show the following trend in terms of reactivity: $MgH_2 < SrH_2 < LiH \approx CaH_2 \approx BaH_2 < NaH$. The order of the reductants are discussed in terms of metal electronegativity and bond strengths. NaH and the novel use of SrH_2 allowed for targeted synthesis of reduced Sr_2MnO_{4-x} ($0 \leq x \leq 0.37$) phases. The enhanced control during synthesis demonstrated by this soft chemistry approach has allowed for a more comprehensive and systematic evaluation of Sr_2MnO_{4-x} phases than previously reported phases prepared by high temperature methods. $Sr_2MnO_{3.63(1)}$ has for the first time been shown to be monoclinic by powder X-ray diffraction and the oxidative monoclinic to tetragonal transition occurs at 450 °C.

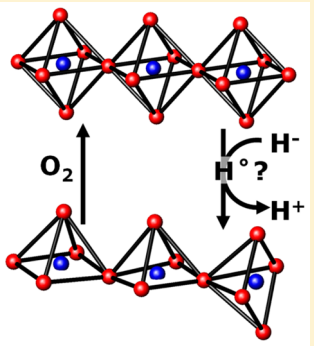

1. INTRODUCTION

Over the past decade the use of metal hydrides as reductants for transition metal oxides has excelled as a soft chemistry technique. Metal hydride reductants have demonstrated advanced mechanistic control for carrying out single-step reductions and multistep reduction/insertion reactions.[1−5] While current literature illustrates the successful synthesis of many novel oxygen defect structures, there are a number of fundamental challenges that remain unexplored. This includes identification of the active reducing species (e.g., H^-, H_2) and the number of electrons that the species contribute to reduction.

When using metal hydrides a number of reducing species might be encountered. The metal hydride can act as a hydride transfer agent, where the H^- anion acts as a reductant in the solid state. Alternatively, the metal hydride can decompose at elevated temperatures and may deliver H_2 gas and the associated metal. Both of those can act as reductants.

The metal hydride reduction mechanism is not well understood; however, it has been shown to occur via diffusion between solids in $LaNiO_2$.[1] Bridges et al. proposed a hopping mechanism of hydride anions in the perovskite layers and determined diffusion coefficients for hydride ions in $LaSrCoO_3H_{0.7}$.[6] Furthermore, reduction can occur via in-situ-generated H_2 gas. Kobayashi et al. pointed out that the gas-phase contribution to the reduction is slower than direct H^- reduction and that sample workup can be avoided with this method. If both mechanisms contribute the hydride diffusion will dominate.[7] Also, no systematic metal hydride reductant reactivity has been characterized to date. The lack of rationalization for the choice of metal hydrides used in the current literature emphasizes the importance of understanding the mechanism of metal hydride reductions. There is the need for both characterization of NaH, CaH_2, and LiH reactivity as used in current literature and also a broader assessment of group I and II metal hydride reductant reactivity to promote further growth of this soft chemistry technique.

The first goal was to identify a representative system suitable for characterizing the metal hydride reduction mechanism and reactivity. Ideally this structure should be stable enough to permit topotactic reductions at low and intermediate temperatures, thus permitting the synthesis of novel oxygen defect phases. Ruddlesden−Popper (RP) phases ($A_{(n+1)}B_nO_{(3n+1)}$) with $n = 1 (A_2BO_4)$ are excellent model compounds as previously shown with many successful metal hydride reductions reported for these structures.[4,5] In particular, the RP $n = 1$ phases are tolerant toward oxygen defects and provide a variety of oxide ion migration mechanisms.[8,9] Sr_2MnO_4 is a suitable starting material for the systematic characterization of the metal hydride reduction mechanism and reactivity. Sr_2MnO_4 is isostructural with K_2NiF_4 and crystallizes in space group *I*4/*mmm* (No. 139). The Sr_2MnO_4 structure is formally an intergrowth of alternating SrO rock salt (R) and $SrMnO_3$ perovskite (P) layers with two distinct oxygen positions on the *4c* and *4e* sites. Figure 1a emphasizes the 9-fold-coordinated strontium ions (*site 4e*) and the 6-fold octahedral coordination of manganese (*site 2a*). The corner-sharing Mn−O_6 octahedra form a two-dimensional sublattice in the *ab* plane via the *4c* oxide site.[10,11]

Gillie et al.[12] proposed a monoclinic defect superstructure based on their neutron data for $Sr_2MnO_{3.64}$, a two-dimensional

Received: December 8, 2014
Published: April 20, 2015

DOI: 10.1021/ic502932x
Inorg. Chem. 2015, 54, 4249−4256

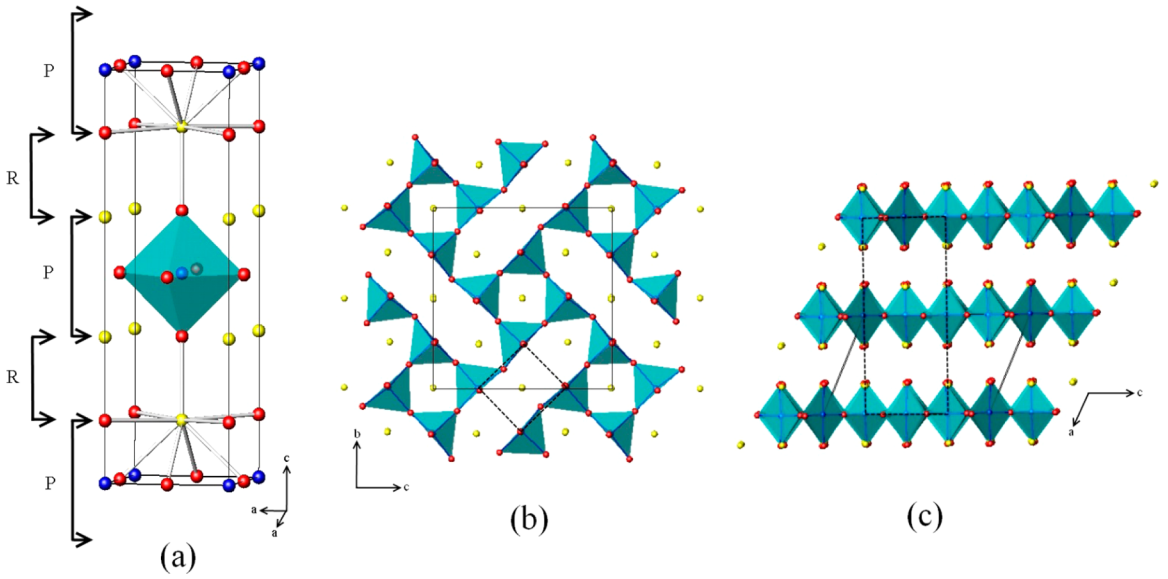

Figure 1. (a) Sr_2MnO_4 n = 1 Ruddlesden−Popper structure. "R" and "P" denote rock salt and perovskite layers, respectively. (b) Monoclinic $Sr_2MnO_{3.5}$ structure viewed down the a axis. (c) $Sr_2MnO_{3.5}$ structure viewed down the b axis. In b and c the solid black lines show the monoclinic unit cell, and the dashed black lines indicate the corresponding tetragonal Sr_2MnO_4 subcell. Yellow, strontium; blue, manganese; red, oxygen.

equivalent of Sr_2MnO_4 consisting of corner-sharing Mn−O_5 square pyramids. A schematic of the hypothetically fully reduced $Sr_2MnO_{3.5}$-type structure is shown in Figure 1b and 1c. The reduced monoclinic oxide defect superstructure should be accessible via topotactic reductions of Sr_2MnO_4.

Current literature demonstrates the use of LiH, NaH, and CaH_2 reductants.[1,4,5,13−20] In this study the reactivity of LiH, NaH, CaH_2, and novel MgH_2, SrH_2, and BaH_2 reductants are characterized. We illustrate how understanding metal hydride reactivity can be utilized for the controlled synthesis of targeted reduced phases, Sr_2MnO_{4-x} ($0 \le x \le 0.37$). In the past the oxygen defect phases Sr_2MnO_{4-x} (x = 0.16, 0.28, 0.36) were prepared by high-temperature reductions in hydrogen flow; this approach yielded different oxygen defect concentrations but did not provide control in order to obtain specific defect phases.[12,21−23] Compositions with x = 0.16 and 0.28 retain the ideal tetragonal ($I4/mmm$) unit cell with statistical oxygen defects (∼8% and ∼14%, respectively) on the equatorial (0, 0.5, 0) oxygen $4c$ site. This results in corner-sharing square pyramidal Mn−O_5 polyhedra within the perovskite layers. The further increase of oxide defects on the original $4c$ site for compositions x = 0.36 results in a monoclinic ($P2_1/c$) structure. In $Sr_2MnO_{3.64}$ 77% of the equatorial oxygen site are now oxygen vacancies. In contrast to the monoclinic $Sr_2MnO_{3.5+x}$ oxide defect phase the analogous layered $Ca_2MnO_{3.5}$ and the 3-dimensional $CaMnO_{2.5}$ and $SrMnO_{2.5}$ oxide defect phases crystallize in orthorhombic structures.[24,25]

We report the targeted and highly reproducible synthesis of Sr_2MnO_{4-x} oxide defect structures using LiH, NaH, MgH_2, CaH_2, SrH_2, and BaH_2 as solid-state metal hydride reductants at low temperatures. The systematic comparison of all six metal hydrides, hydrogen gas, as well as alkali metals for Sr_2MnO_4 reductions results in identification of the reducing species during the reactions. All reduction pathways as a function of the metal hydrides are presented. The structural analysis of all reduced phases is provided, and the structural evolution during oxidation of $Sr_2MnO_{3.63}$ is followed in detail.

2. EXPERIMENTAL SECTION

2.1. Sr_2MnO_4 Synthesis. Polycrystalline bulk (∼6 g) Sr_2MnO_4 samples were prepared by solid-state synthesis according to eq 1. Stoichiometric quantities of $SrCO_3$ (Alfa Aesar, 99.99%) and Mn_2O_3 (CERAC, 99.9%) were ground in an agate mortar with acetone and heated for 72 h (24 h, regrind, 48 h) in static air at 1300 °C followed by heating for 30 min at 1500 °C in N_2 and quenching in air. The product is black polycrystalline Sr_2MnO_4 with typically 1−2% of $Sr_3Mn_2O_7$ impurity as determined by powder X-ray diffraction.

$$4SrCO_3 + Mn_2O_3 + 1/2O_2 \rightarrow 2Sr_2MnO_4 + 4CO_2 \quad (1)$$

2.2. Metal Hydride Reductions. Metal hydride reductions of Sr_2MnO_4 have been carried out using NaH (Sigma-Aldrich, 90−95%), LiH (Sigma-Aldrich, 95%), MgH_2 (Alfa Aesar, 98%), CaH_2 (Sigma-Aldrich, 90−95%), SrH_2 (CERAC, 99.5%), and BaH_2 (CERAC, 99.7%).

Note: All of these metal hydrides are strong reductants and strong bases capable of igniting in air and releasing hydrogen gas upon exposure to water. MSDS sheets need to be consulted, and caution needs to be exercised when working with metal hydrides.

Sr_2MnO_4 (200 mg) is ground in an agate mortar with a 4-fold stoichiometric excess (with respect to reduction to $Sr_2MnO_{3.5}$, i.e., x = 0.5) of the metal hydride reductant according to eqs 2 and 3 [Y = Li, Na; Z = Mg, Ca, Sr, Ba] in an N_2-filled MBraun Unilab glovebox (O_2 < 1 ppm). The reaction mixture is transferred to a pyrex ampule and sealed under vacuum. Reactions have been carried out at specific temperatures between 100 and 600 °C for 24 h. Soluble excess metal hydride, metal oxide, and metal hydroxide byproducts are dissolved in 6 × 10 mL of 0.1 M NH_4Cl in methanol and filtered off.

$$Sr_2MnO_4 + (x)YH \rightarrow Sr_2MnO_{4-x} + (x)YOH \quad (2)$$

$$Sr_2MnO_4 + (x/2)ZH_2 \rightarrow Sr_2MnO_{4-x} + (x/2)Z(OH)_2 \quad (3)$$

2.3. Metal Reductions. Reduction of Sr_2MnO_4 was attempted using Na metal as a reducing agent. Sr_2MnO_4 (200 mg) was combined in a glovebox (O_2 < 1 ppm) with a 2-fold molar Na metal excess. Reaction mixtures were transferred to pyrex ampules and sealed under dynamic vacuum. Ampules were heated at specific temperatures between 100 and 600 °C for 24 h.

2.4. Room-Temperature Powder X-ray Diffraction. All products were identified using a PANalytical X'Pert Pro powder X-ray diffractometer with Cu $K\alpha_{1,2}$ (λ = 1.540598 Å, 1.544426 Å)

DOI: 10.1021/ic502932x
Inorg. Chem. 2015, 54, 4249−4256

radiation equipped with a diffracted beam Ni filter and an X'Celerator detector operated in Bragg–Brentano geometry. Room-temperature diffractograms were collected from 10° to 120° (2θ) with a step size of 0.0083°. Phase identification (using PDF2003) was carried out with X'Pert Highscore Plus (2.1. version). Powder X-ray diffraction Rietveld refinements were carried out using FullProf 2008.[26]

2.5. High-Temperature Powder X-ray Diffraction. High-temperature powder X-ray diffraction experiments were carried out on a PANalytical X'Pert Pro diffractometer equipped with an X'Celerator detector and an Anton Paar HTK2000 high-temperature camera. Polycrystalline $Sr_2MnO_{3.63(1)}$ was heated on a resistive platinum strip heater from 25 to 600 °C in static air. Using Cu $K\alpha_{1,2}$ (λ = 1.540598 and 1.544426 Å) radiation diffraction patterns were collected in 25 °C increments covering the angular range 18° ≤ 2θ ≤ 22° with 0.0083° step size.

2.6. Rietveld Refinements. Powder X-ray diffraction Rietveld refinements for tetragonal Sr_2MnO_{4-x} (x < 0.37) phases allowed for full refinement of the zero point, unit cell parameters, peak shape parameters, and background points interpolated with a cubic spline. For the tetragonal phases all atomic positions and temperature factors were refined. For the monoclinic phases only the strontium positions were refinable.

2.7. Thermogravimetric Analysis/Differential Thermal Analysis (TGA/DTA). Thermogravimetric analysis (TGA) experiments were carried out with a Netzsch STA 409 thermobalance. Sr_2MnO_{4-x} ($0 \le x \le 0.37$) samples (approximately 50 mg) were heated from 25 to 800 °C in oxygen flow with a heating rate of 5 °C/min. Buoyancy corrections were applied to all experimental data. All products were identified by powder X-ray diffraction. Simultaneous TGA/DTA measurement for the oxidation in static air of $Sr_2MnO_{3.63(1)}$ (approximately 50 mg) was carried out on a Linseis L81 thermobalance using a heating rate of 5 °C/min from 25 to 600 °C. Buoyancy corrections were applied.

3. RESULTS AND DISCUSSION

3.1. Solid-State NaH vs H_2 Gas Flow. Comparing reductions of Sr_2MnO_4 using NaH and hydrogen gas provides motivation for the use of metal hydride reductants. Reduction of Sr_2MnO_4 was evaluated by monitoring the unit cell volumes as a function of reaction temperature. This approach was used consistently throughout this study and thus enabled the construction of reduction trends which provides insight into reductant reactivity and the extent of reduction. Reduction of Mn^{4+} to Mn^{3+} causes the unit cell volume to increase. The benefits of using NaH over H_2 gas has been shown in the reduction of $LaSrCoO_4$[27] and has been explored further for the reduction of Sr_2MnO_4. Figure 2 emphasizes the benefit of using metal hydride reductants over hydrogen gas. NaH reduces Sr_2MnO_4 at temperatures as low as 150 °C, while the onset for reduction in pure and 50% H_2 flow is observed at 300 and 400 °C, respectively. Notably, the volume plateau (91.75–91.95 Å^3) reached by both NaH and hydrogen gas agrees well with the published volume of 91.96(1) Å^3 for $Sr_2MnO_{3.64(2)}$.[12] The data points at 300 °C indicate that NaH produces the most reduced phase (~$Sr_2MnO_{3.6}$), while pure H_2 produces an intermediate reduced phase, and 50% H_2 flow only causes negligible reduction. NaH is a more reactive reductant than H_2, and this promotes enhanced kinetic control for carrying out controllable reductions using H^- as a solid-state reductant at low temperatures. Furthermore, direct reaction with sodium metal up to 600 °C did not show any significant reduction. Therefore, the metal which is potentially present after hydride decomposition does not contribute to the reduction of Sr_2MnO_4.

3.2. Investigation of Reduction Mechanism. Kobayashi et al.[7] discuss a one- vs two-electron transfer for CaH_2 and NaH

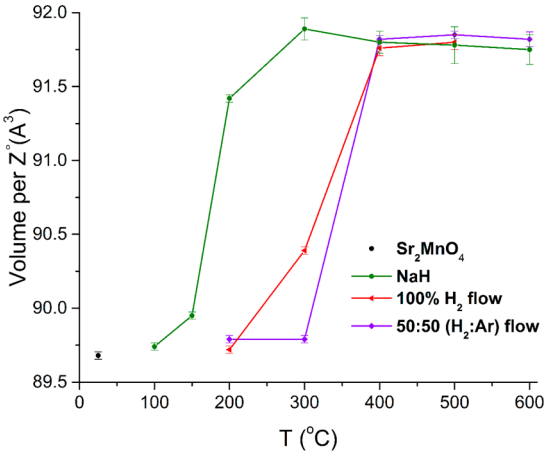

Figure 2. Comparison of Sr_2MnO_4 reductions for solid NaH and variable concentrations of flowing hydrogen gas.

in terms of lattice enthalpies, equilibrium constants, and thermodynamics of their byproducts; however, there are yet to be laboratory experiments supporting these discussions. We report a stoichiometric approach for metal hydride reductions of Sr_2MnO_4 to gain critical information regarding the H^- reduction mechanism. Identifying the stoichiometric ratio (Sr_2MnO_4:MH) required for the synthesis of the most reduced phase ($Sr_2MnO_{3.63}$) has provided proof that H^- is donating more than one electron in the reduction. The described determination of H^- as the dominant reducing species and the following evidence that H^- donates multiple electrons aids in the understanding of an otherwise unknown reaction mechanism. Case studies for LiH and CaH_2 have been carried out (Figures 3 and 4) by plotting the volumes per formula unit

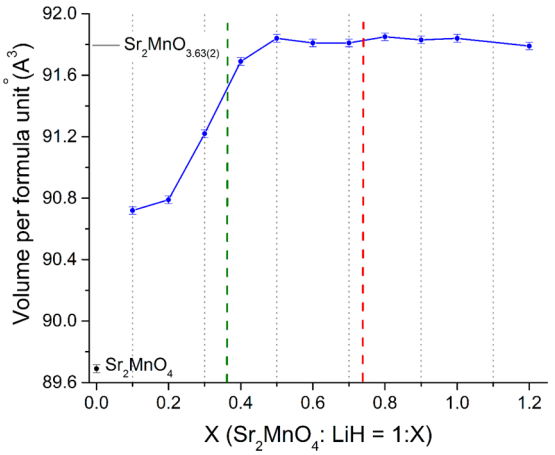

Figure 3. Volume per formula unit (Sr_2MnO_4) as a function of LiH stoichiometry. Reactions occur in a sealed ampule at 400 °C. Data at X = 0 corresponds to the starting material (Sr_2MnO_4) volume. Green dashed line represents the limit for a two-electron process; red dashed line represents the limit for a one-electron process.

(Sr_2MnO_4) as a function of metal hydride reaction stoichiometry. The findings are discussed with respect to eqs 4 and 5.

$$Sr_2MnO_4 \xrightarrow{LiH/400\,^\circ C} Sr_2MnO_{3.63} \quad (4)$$

$$Sr_2MnO_4 \xrightarrow{CaH_2/400\,^\circ C} Sr_2MnO_{3.63} \quad (5)$$

DOI: 10.1021/ic502932x
Inorg. Chem. 2015, 54, 4249–4256

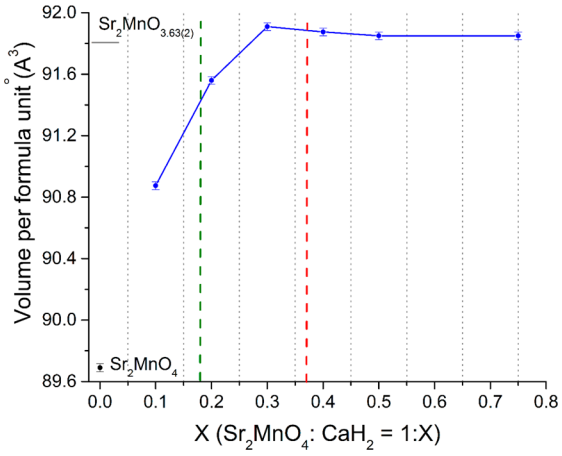

Figure 4. Volume per formula unit (Sr_2MnO_4) as a function of CaH_2 stoichiometry. Reactions occur in a sealed ampule at 400 °C. Data at X = 0 corresponds to the starting material (Sr_2MnO_4) volume. Green dashed line represents the limit for a two-electron process; red dashed line represents the limit for a one-electron process.

In these reaction schemes it is clear that manganese is being reduced from Mn(IV) to a mixture of Mn(IV) and Mn(III). In the case of the reduction to $Sr_2MnO_{3.63}$ a ratio of approximately 1:3 (Mn(IV):Mn(III)) is seen. If each hydride ion only donates one electron ($H^- \rightarrow H^\bullet$), reducing 1 mol of Sr_2MnO_4 to $Sr_2MnO_{3.63}$ should require a minimum of 0.74 mol of LiH or 0.37 mol of CaH_2, respectively, whereas if each hydride ion donates two electrons ($H^- \rightarrow H^+$) the reduction would require a minimum of 0.37 mol of LiH or 0.185 mol of CaH_2.

Figures 3 and 4 illustrate the reduction of Sr_2MnO_4 with LiH and CaH_2, respectively, at 400 °C in sealed ampules. The most reduced phase $Sr_2MnO_{3.63}$ ($V \approx 91.8$ Å^3) is obtained with $a \leq$ 0.5 LiH to 1 Sr_2MnO_4 ratio, significantly less than the 0.74 LiH required for a one-electron reduction ($H^- \rightarrow H^\bullet$). This is further supported by obtaining $Sr_2MnO_{3.63}$ with ≤0.3 CaH_2 rather than the expected 0.37 CaH_2 required for a one-electron reduction. Consequently, more than one electron is provided by H^- during the reduction of Mn^{4+} to Mn^{3+} under those conditions. It should be realized that specific mechanistic details for the conversion of H^-/H^+ cannot be provided; however, a simple one-electron process can be ruled out. This leaves multiple reduction mechanisms for the reduction of Sr_2MnO_4 to $Sr_2MnO_{3.63}$, which involves the transfer of 0.74 electrons as indicated in the half reaction in eq 6.

$$Sr_2MnO_4 \xrightarrow{0.74e^-} Sr_2MnO_{3.63} \quad (6)$$

There are two consecutive one-electron transfers where the reduction occurs via oxidation of H^- to an $H^\bullet$ radical and proceeds via $H^\bullet$ to H^+ as shown in eqs 7a and 7b. Note that the stoichiometric coefficients are used according to eq 6.

$$0.37H^- \xrightarrow{1e^-} 0.37H^\bullet \quad 0.37e^- \text{ transferred} \quad (7a)$$

$$0.37H^\bullet \xrightarrow{1e^-} 0.37H^+ \quad 0.37e^- \text{ transferred} \quad (7b)$$

$$0.37H^- \xrightarrow{2e^-} 0.37H^+ \quad 0.74e^- \text{ transferred} \quad (8)$$

Alternatively, a concerted two-electron transfer may be considered where H^- is oxidized directly to H^+, eq 8. The reaction products for both reactions are indistinguishable. Excess hydride during the reduction will generate H_2 gas and protons; however, when reaching 2-fold excess no protons will be observed in the product (see Supporting Information). Notably, the reduction of Sr_2MnO_4 to $Sr_2MnO_{3.63}$ required >0.37 LiH, indicating potential side reactions which cause the formation of H_2. Since the solid-state hydride reductions assume hydride diffusion into the host lattice (e.g., Sr_2MnO_4) low local hydride/hydrogen radical concentrations are expected during the reaction. However, the occasional encounter of 2 $H^\bullet$ or an H^- and H^+ in the lattice allows for H_2 formation. This can explain the presence of H_2, which is seen via the pressurized ampules even below the decomposition temperature of the metal hydride. Figures 3 and 4 indicate for the Sr_2MnO_4 reduction a 75% hydride yield with the remaining 25% forming H_2 gas in a side reaction. Illustrations of the reactions for a slight excess can be seen in the Supporting Information. Although the exact reduction mechanism is still unclear, it is clear that more than one electron per H^- is being donated to the metal. These findings are a step forward in understanding the mechanistic details of these unconventional reactions.

3.3. Characterization of Metal Hydride Reactivity. We report for the first time the characterization of metal hydride reductant reactivity. Evaluating the unit cell evolution of Sr_2MnO_4 reduction products allows for determination of reduction trends for all six metal hydrides (LiH, NaH, MgH_2, CaH_2, SrH_2, and BaH_2). Figure 5 shows the formula unit

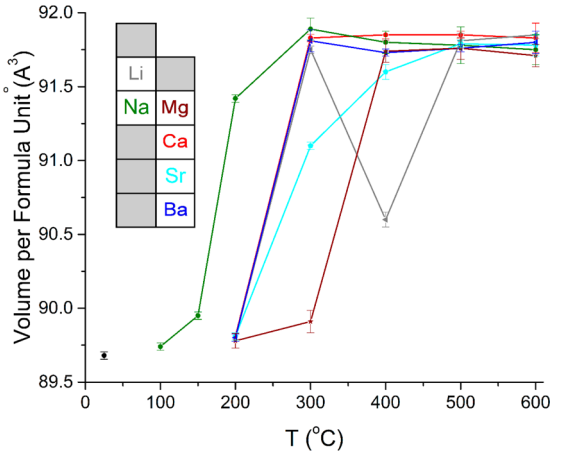

Figure 5. Volume per formula unit (Sr_2MnO_4) as a function of reaction temperature (100−600 °C) for LiH, NaH, MgH_2, CaH_2, SrH_2, and BaH_2. Colors of the data match the color legend on the left. The data point at 25 °C corresponds to the unreduced starting material.

volumes as a function of reaction temperature and reveals striking differences in metal hydride reactivity. A range of reduction onset temperatures and different reduction temperature ranges is observed, suggesting a varying degree of control for solid-state hydride reductions as a function of metal hydride. NaH is the only metal hydride capable of significantly reducing Sr_2MnO_4 below 200 °C, making it the most reactive reductant explored. Reductions with MgH_2 initiate at higher temperatures (≥400 °C) than all other hydrides, making MgH_2 the least reactive metal hydride. LiH, CaH_2, and BaH_2 have very similar reduction trends with intermediate reactivity in comparison to NaH and MgH_2 with overlapping trends between 200 and 300 °C. SrH_2 reductions initiate at temperatures just below those observed for MgH_2 to give an overall reactivity trend of MgH_2 < SrH_2 < LiH ≈ CaH_2 ≈ BaH_2 < NaH. This is the first reported

DOI: 10.1021/ic502932x
Inorg. Chem. 2015, 54, 4249−4256

systematic characterization of reactivity for metal hydride solid-state reductants. Explanation of the observed reactivity among group I and II metal hydrides appears to be complex. This is anticipated due to the number of factors that can influence metal hydride reactivity such as decomposition temperatures, metal hydride structure, electronic considerations (e.g., cation electronegativity χ and bond strength), and thermodynamic factors such as enthalpy of formation (ΔH_f°). There appears to be a relationship between cation electronegativity and reactivity. This is most notable when comparing NaH (χ = 0.93) and MgH_2 (χ = 1.31) in which magnesium has the highest cation electronegativity and is the least reactive while sodium with the lowest cation electronegativity is the most reactive hydride. This is consistent with LiH, CaH_2, BaH_2, and SrH_2 having cations with intermediate electronegativities (~1) reflected by their intermediate reactivity to NaH and MgH_2. This suggests that the ionicity of the metal hydrides is important for gauging hydride anion reactivity. This observation might be coincidental, and the observed reactivities may actually result from a complex interplay of the factors mentioned above. A number of additional interesting features are present in Figure 5. The LiH reduction product at 400 °C appears as a drastic and unexpected volume decrease compared to the 300 and 500 °C products. This product results from anisotropic unit cell dimension changes (*a* axis ↓0.35%, *c* axis ↑ 1.4%). This is unusual as all other reduction products shown in Figure 5 result from isotropic unit cell changes (*a*,*c* axis ↑). This is strong evidence that the LiH product at 400 °C is not simply a reduced phase but that more complex processes are involved. A detailed investigation of the LiH reductions will be reported elsewhere. It should be noted that SrH_2 provides excellent control for solid-state hydride reductions as indicated by the gentle slope for its reduction trend in Figure 5. To our knowledge SrH_2 has not been used for solid-state reductions of oxides in the past. SrH_2 is a particularly appealing metal hydride reductant. Both NaH and SrH_2 stand apart from the remaining metal hydrides tested due to their gradual and overall gently sloped reactivity trends as a function of temperature. Optimized reduction conditions adapted directly from the NaH and SrH_2 reduction trends in Figure 5 have been used to carry out targeted synthesis of reduced phases.

3.4. Targeted Synthesis of Reduced Phases. Extrapolating temperatures from the NaH and SrH_2 reduction trends shown in Figure 5 allowed for the synthesis of targeted reduced phases Sr_2MnO_{4-x} ($0 \le x \le 0.37$) as shown in Figure 6. All oxygen stoichiometries shown in Figure 6 have been determined by thermogravimetric oxidation of the reduced phases. This demonstrates the use of metal hydrides for the controlled synthesis of specific reduced phases. It is clear from Figure 6 that the systematic approach of tunable metal hydride reductions is much more effective at surveying the oxygen defect phases of Sr_2MnO_4 than high-temperature gas flow reductions. With the exception of the published $Sr_2MnO_{3.72}$ phase[22] all reduction products follow an almost linear unit cell volume vs oxygen stoichiometry relation. The ability to extrapolate reaction temperatures from Figure 6 to carry out targeted synthesis emphasizes the reproducibility and reliability of the established reduction trends. Oxidation of all reduced phases is observed to begin between 250 and 300 °C. If desired any composition of Sr_2MnO_{4-x} ($0 \le x \le 0.37$) can be synthesized by tuning reaction conditions. This combination of well-characterized reaction conditions and structural stability provides optimal conditions for understanding the complete

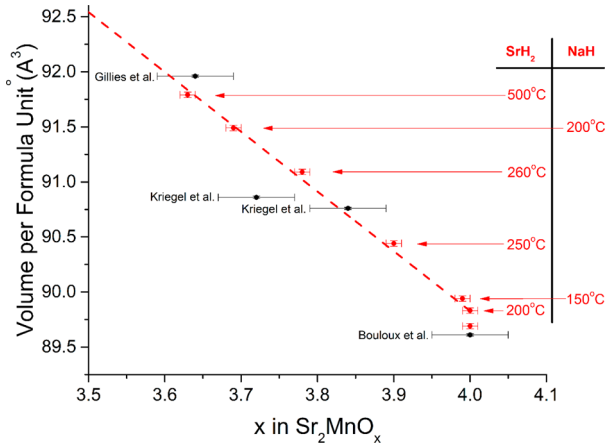

Figure 6. Volume per formula unit evolution comparing the previously published[11,12,21,22] Sr_2MnO_{4-x} phases (gray) with those synthesized using SrH_2 and NaH (red); synthesis conditions are indicated on the right.

structure–property relationship that the Sr_2MnO_{4-x} ($0 \le x \le 0.37$) phases have to offer. Applying this approach to novel systems could prove to be invaluable in terms of exploiting a system's structure–property relationship.

3.5. Sr_2MnO_{4-x} ($0 \le x \le 0.37$) Structure Analysis. $Sr_2MnO_{3.72(5)}$,[22] $Sr_2MnO_{3.84(5)}$,[21] and Sr_2MnO_4[11] have been published as tetragonal (*I4/mmm*) Sr_2MnO_4-type oxide defect structures. This is consistent with our findings that $Sr_2MnO_{3.69(1)}$ is tetragonal with no indication of any monoclinic superstructure peaks in the X-ray diffractograms. The Rietveld plot of tetragonal $Sr_2MnO_{3.69(1)}$ prepared with NaH is shown in Figure 7, and the refined crystallographic parameters are listed in Table 1. Notably, Gillie et al.[12] provided a preliminary refinement for $Sr_2MnO_{3.64}$ using the tetragonal model (*I4/mmm*) for their powder X-ray diffraction data. The final refinement for the same sample using powder neutron data was carried out using the monoclinic defect superstructure ($P2_1/c$), revealing the structural details including disordered excess

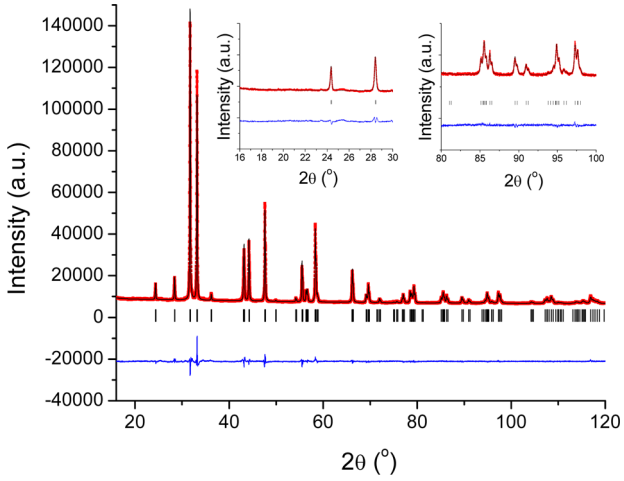

Figure 7. Room-temperature Rietveld plot for tetragonal $Sr_2MnO_{3.69(1)}$ using powder X-ray diffraction data (Cu K$\alpha_{1,2}$). (Insets) Selected low-angle and high-angle regions. Note the absence of monoclinic superstructure peaks at low angles. Red symbols = experimental data, black line = calculated pattern, blue line = difference, black markers = Bragg positions.

DOI: 10.1021/ic502932x
Inorg. Chem. 2015, 54, 4249–4256

Table 1. Structural Parameters for the Tetragonal $Sr_2MnO_{3.69(1)}$ Ruddlesden–Popper Phase (space group *I*4/*mmm* (No. 139)) As Obtained from Rietveld Refinement Against X-ray Diffraction Data Measured at Room Temperature[a]

composition		$Sr_2MnO_{3.69(1)}$
space group		*I*4/*mmm* (No. 139)
unit cell	*a* (Å)	3.8167 (2)
	c (Å)	12.5606 (7)
	V (Å^3)	182.97 (2)
	z/*c*	0.3542 (2)
Sr (4e) (0, 0, *z*)	B_{iso} (Å^2)	0.55 (5)
Mn (2a) (0, 0, 0)	B_{iso} (Å^2)	0.28 (6)
O (4c) (0, 0.5, 0)	B_{iso} (Å^2)	3.5 (4)
O (4e) (0, 0, *z*)	*z*/*c*	0.1556 (9)
	B_{iso} (Å^2)	0.9 (2)
no. of params		24
Z		2
R values	XRD:[b] (Rp, Rwp, χ^2)	1.89/2.71/6.55

[a]Note that oxygen composition has been determined by TGA and is not refined from X-ray diffraction data due to lack of sensitivity. Only the manganese site occupancy was refined. [b]X-ray: $K_{\alpha 1,2}$, λ = 1.540598 and 1.544426 Å, 15° ≤ 2θ ≤ 120°, $\Delta 2\theta$ = 0.0083°, 13 159 data points.

oxygen. This has possibly lead to some confusion regarding the structure and composition in the recent literature. The Rietveld plot of our $Sr_2MnO_{3.63(1)}$ sample synthesized using SrH_2 is shown in Figure 8, and the crystallographic data are provided in

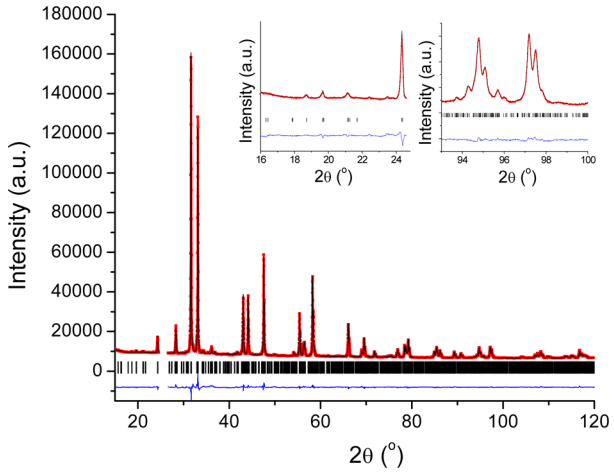

Figure 8. Room-temperature Rietveld plot for monoclinic $Sr_2MnO_{3.63(1)}$. Powder X-ray diffraction data Cu $K\alpha_{1,2}$ (Bragg *R* factor = 4.20). Low-angle (monoclinic superstructure peaks) and high-angle insets. A broad peak unrelated to the monoclinic structure at 25.3° was excluded from the refinement. Red symbols = experimental data, black line = calculated pattern, blue line = difference, black markers = Bragg positions.

Table 2. The monoclinic superstructure peaks are readily identifiable between 18° and 22° (2θ) in the inset of Figure 8. A 22 h (1500 s/step; 0.0083° steps) data collection time was required to clearly show the monoclinic superstructure peaks. Thus, it is expected that previously published X-ray data missed the monoclinic superstructure peaks for this phase due to insufficient counting statistics. Monoclinic superstructure peaks are only observed for Sr_2MnO_{4-x} ($x \geq 0.37$); thus, all phases with $x < 0.37$ are tetragonal. Notably, high-temperature X-ray

Table 2. Structural Parameters for the Monoclinic $Sr_2MnO_{3.63(1)}$ Ruddlesden–Popper Phase (space group $P2_1/c$ (No. 14)) As Obtained from Rietveld Refinement Against X-ray Diffraction Data Measured at Room Temperature[a]

composition		$Sr_2MnO_{3.63(1)}$
space group		$P2_1/c$ (No. 14)
unit cell	*a* (Å)	6.8446 (4)
	b (Å)	10.8008 (9)
	c (Å)	10.804 (1)
	β (deg)	113.18 (1)
	V (Å^3)	734.3 (1)
Sr1 (4e) (*x*,*y*,*z*)	*x*/*a*	0.286 (4)
	y/*b*	−0.007 (3)
	z/*c*	0.073 (5)
Sr2 (4e) (*x*,*y*,*z*)	*x*/*a*	0.306 (2)
	y/*b*	−0.001 (3)
	z/c	0.575 (5)
Sr3 (4e) (*x*,*y*,*z*)	*x*/*a*	0.286 (5)
	y/*b*	0.243 (3)
	z/*c*	0.332 (4)
Sr4 (4e) (*x*,*y*,*z*)	*x*/*a*	0.295 (5)
	y/*b*	0.744 (3)
	z/*c*	0.317 (6)
Mn1 (4e) (*x*,*y*,*z*)	*x*/*a*	−0.017 (9)
	y/*b*	0.001 (3)
	z/*c*	0.246 (7)
Mn2 (4e) (*x*,*y*,*z*)	*y*/*a*	−0.012 (8)
	z/*b*	0.251 (5)
	x/*c*	0.003 (4)
excluded region	1	24.6° ≤ 2θ ≤ 26.6°
no. of params		51
Z		8
R values	XRD:[b] (Rp, Rwp, χ^2)	1.31/1.96/34.8

[a]Note that B_{iso}(Sr1) = B_{iso}(Sr2) = B_{iso}(Sr3) = B_{iso}(Sr4) = 0.37(8) Å^2, B_{iso}(Mn1) = B_{iso}(Mn2) = 0.08(7) Å^2, and B_{iso}(O1)...B_{iso}(O8) = 0.4(2) Å^2. Oxygen postions were fixed to the values reported by Gillie et al.[12] The oxygen stochiometry has been determined by TGA and is not refined from X-ray diffraction data due to lack of sensitivity. [b]X-ray: $K_{\alpha 1,2}$, λ = 1.540598 and 1.544426 Å, 15° ≤ 2θ ≤ 120°, $\Delta 2\theta$ = 0.0167°, 6576 data points.

diffraction studies for monoclinic $Sr_2MnO_{3.63(1)}$ under gently reducing conditions (CO:He = 1:9) showed that there is no structural transition to tetragonal symmetry at high temperature. Instead, decomposition into MnO and SrO is observed at temperatures greater than 850 °C. In-situ oxidation of $Sr_2MnO_{3.63(1)}$ as shown in the inset in Figure 9 shows the disappearance of the monoclinic superstructure peaks at 450 °C, marking the oxidative transition temperature from monoclinic to tetragonal. The TGA/DTA data shown in Figure 10 for the oxidation of $Sr_2MnO_{3.63}$ support the oxidative structural change from monoclinic to tetragonal where the oxygen uptake is accompanied by an endothermic DTA signal.

4. SUMMARY AND CONCLUSIONS

We provide a comprehensive investigation of the metal hydride reduction mechanism, metal hydride reactivity, and ability to carry out targeted reductions of Sr_2MnO_4 using metal hydrides. The motivation for using metal hydrides to carry out controllable reductions is made clear by their reactivity at considerably lower temperatures than that of conventional reductants such as hydrogen gas. Direct reduction of Sr_2MnO_4 by metals has been ruled out. The reaction mechanism of these

DOI: 10.1021/ic502932x
Inorg. Chem. 2015, 54, 4249–4256

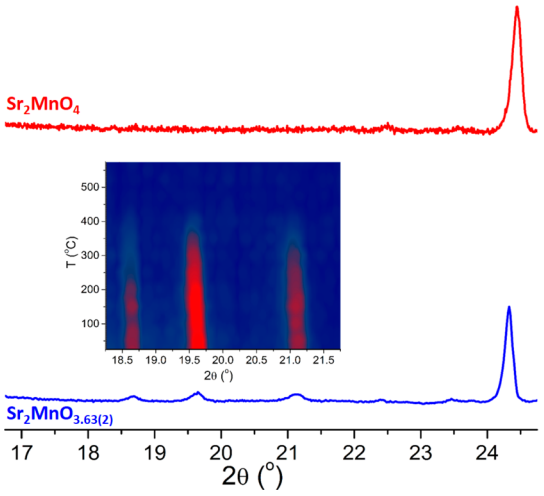

Figure 9. Powder X-ray diffraction patterns of monoclinic $Sr_2MnO_{3.63(1)}$ (blue) and tetragonal Sr_2MnO_4 (red). (Inset) Powder X-ray diffraction contour plot of monoclinic $Sr_2MnO_{3.63(1)}$ oxidation in O_2 flow from 25 to 575 °C with 25 °C increments. The color transition from blue to red indicates intensity increases.

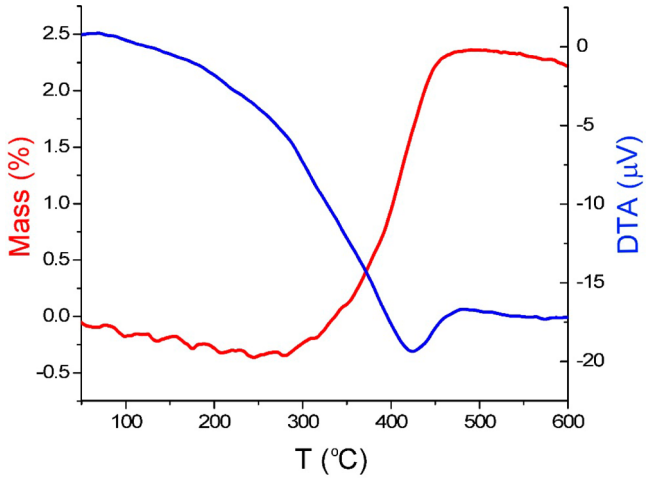

Figure 10. Simultaneous TGA and DTA data for the oxidation of monoclinic $Sr_2MnO_{3.63}$ to tetragonal Sr_2MnO_4 in static air.

hydride reductions has been investigated, and hydride anions have been found to donate more than one electron during reduction. Novel reactivity trends have been constructed which provide valuable information about metal hydride reactivity. The reactivity trend for the 6 metal hydrides when reducing Sr_2MnO_4 is as follows: $MgH_2 < SrH_2 < LiH \approx CaH_2 \approx BaH_2 <$ NaH. Identifying the reactivity trends of these 6 metal hydrides provides more control for low-temperature reductions. The synthesis of novel defect structures will benefit from the selectivity and better kinetic control provided by this series. The use of NaH and SrH_2 allowed for the synthesis of targeted reduced phases, Sr_2MnO_{4-x} ($0 < x < 0.37$), by using reduction conditions established from reactivity trends. The ability to extrapolate reaction conditions reinforced the reliability and reproducibility of this synthetic technique.

■ ASSOCIATED CONTENT

Ⓢ Supporting Information

Electron transfer equations. This material is available free of charge via the Internet at http://pubs.acs.org.

■ AUTHOR INFORMATION

Corresponding Author

*Phone: (204) 474-6258. Fax: (204) 474-7608. E-mail: Mario_Bieringer@umanitoba.ca.

Author Contributions

‡Joey A. Lussier and Bradley C. Hernden contributed equally to this work.

Notes

The authors declare no competing financial interest.

■ ACKNOWLEDGMENTS

The authors thank F. Gibbs (Brockhouse Institute for Materials Research) for help with the TGA data, V. Michaelis and S. Kroeker for access to the high-temperature furnace laboratory, and P. Budzelaar for insightful discussions. M.B. acknowledges financial support from NSERC and CFI for operating and infrastructure support. B.C.H. and J.A.L. are thankful for financial support from the University of Manitoba.

■ REFERENCES

(1) Hayward, M. A.; Green, M. A.; et al. *J. Am. Chem. Soc.* **1999**, *121*, 8843−8854.
(2) Hayward, M. A.; Lockett, M. A.; et al. *Inorg. Chem.* **2008**, *47*, 5212−5217.
(3) Bridges, C. A.; Darling, G. R.; Hayward, M. A.; Rosseinsky, M. J. *J. Am. Chem. Soc.* **2005**, *127*, 5996−6011.
(4) Dixon, E.; Hayward, M. A. *Inorg. Chem.* **2010**, *49*, 9649−9654.
(5) Yamamoto, T.; Kageyama, H. *Chem. Lett.* **2013**, *42*, 946−953.
(6) Bridges, C. A.; Fernandez-Alonso, F.; Goff, J. P.; Rosseinsky, M. J. *Adv. Mater.* **2006**, *18*, 3304−3308.
(7) Kobayashi, Y.; Li, Z.; Hirai, K.; Tassel, C.; Loyer, F.; Ichikawa, N.; Abe, N.; Yamamoto, T.; Shimakawa, Y.; Yoshimura, K.; Takano, M.; Hernandez, O. J.; Kageyama, H. *J. Solid State Chem.* **2013**, *207*, 190−193.
(8) Jorgensen, J. D.; Dabrowski, B.; et al. *Phys. Rev. B* **1989**, *40*, 2187−2199.
(9) Stephen, J.; Skinner, J.; et al. *Mater. Today.* **2003**, *March*, 30−37.
(10) Balz, D. *Nautwissenschaften* **1953**, *40*, 241.
(11) Bouloux, J. C.; Soubeyroux, J. L.; et al. *J. Solid State Chem.* **1981**, *38*, 34−39.
(12) Gillie, L. J.; et al. *J. Solid State Chem.* **2002**, *167*, 145−151.
(13) Hayward, M. A.; Lockett, M. A.; et al. *J. Solid State Chem.* **2007**, *180*, 2851−2858.
(14) Hayward, M. A.; Hadermann, J.; et al. *J. Am. Chem. Soc.* **2009**, *131*, 10598−10604.
(15) Hayward, M. A.; Adkin, J. J. *Inorg. Chem.* **2008**, *47*, 10959−10964.
(16) Poltavets, V. V.; Lokshin, K. A.; Dikmen, S.; Croft, M.; Egami, T.; Greenblatt, M. *J. Am. Chem. Soc.* **2006**, *128*, 9050−9051.
(17) Tsujimoto, Y.; Tassel, C.; Hayashi, N.; Watanabe, T.; Kageyama, H.; Yoshimura, K.; Takano, M.; Ceretti, M.; Ritter, C.; Paulus, W. *Nature* **2007**, *450*, 1062−1065.
(18) Kageyama, H.; Watanabe, T.; Tsujimoto, Y.; Kitada, A.; Sumida, Y.; Kanamori, K.; Yoshimura, K.; Hayashi, N.; Muranaka, S.; Takano, M.; Ceretti, M.; Paulus, W.; Ritter, C.; André, G. *Angew. Chem., Int. Ed.* **2008**, *47*, 5740−5745.
(19) Kitchen, H. J.; Saratovsky, I.; Hayward, M. A. *Dalton Trans.* **2010**, *39*, 6098−6105.
(20) Hayward, M. A. *Chem. Mater.* **2006**, *18*, 321−327.
(21) Kriegel, R.; Borrmann, H.; et al. *Z. Naturforsch., B: Chem. Sci.* **1993**, *48b*, 15−18.
(22) Kriegel, R.; Preuß, N. *Thermochim. Acta* **1996**, *285*, 91−98.
(23) Kato, C.; et al. *J. Phys. Soc. Jpn.* **2005**, *74*, 1026−1029.
(24) Poeppelmeier, K. R.; et al. *J. Solid State Chem.* **1985**, *59*, 71−80.
(25) Poeppelmeier, K. R.; Leonowicz, M. E.; et al. *J. Solid State Chem.* **1982**, *45*, 71−79.

DOI: 10.1021/ic502932x
Inorg. Chem. 2015, 54, 4249−4256

(26) Rodriguez-Carvajal, J. *Full Prof 2k*, Version 4.40; 2008.
(27) Hayward, M. A.; Rosseinsky, M. J. *Chem. Mater.* **2000**, *12*, 2185−2192.

DOI: 10.1021/ic502932x
Inorg. Chem. 2015, 54, 4249−4256